

NANO EXPRESS

Open Access



Structural and Morphological Features of Disperse Alumina Synthesized Using Aluminum Nitrate Nonahydrate

Ivan F. Myronyuk¹, Volodymyr I. Mandzyuk^{1*}, Volodymyr M. Sachko¹ and Volodymyr M. Gun'ko²

Abstract

Transformation of $\text{Al}(\text{NO}_3)_3 \cdot 9\text{H}_2\text{O}$ (upon heating in the range of 20–1200 °C) into blends of amorphous and crystalline boehmite (210–525 °C), amorphous alumina and crystalline $\gamma\text{-Al}_2\text{O}_3$ (850 °C), and crystalline $\alpha\text{-Al}_2\text{O}_3$ (1100 °C) was analyzed using X-ray diffraction (XRD), high-resolution transmission electron microscope (HRTEM), infrared (IR) spectroscopy, thermogravimetry, and low-temperature nitrogen adsorption. Boehmite consists of nanoparticles of 6–10 nm in diameter, and part of them has crystalline structure observed in HRTEM images, despite they are XRD amorphous. The nanoglobules are surrounded by amorphous aluminum hydroxide with chains of $-\text{AlO}(\text{H})-\text{O}-\text{AlO}(\text{H})-$ of 1–5 nm in length. Heating of samples at 350–525 °C gives mesoporous aluminum hydroxide with a relatively narrow pore size distribution. An increase in calcination temperature to 850 °C decreases the porosity of alumina composed of amorphous and crystalline ($\gamma\text{-Al}_2\text{O}_3$) phases. Calcination at 1100 °C gives $\alpha\text{-Al}_2\text{O}_3$ with strongly decreased porosity of aggregates.

Keywords: Aluminum nitrate nonahydrate, Aluminum hydroxide, Alumina, Nanoparticle morphology, Aggregate texture

PACS: 61.66.Fn, 64.70.K, 74.62.Bf

Background

Alumina in various modifications, individual crystalline (see Additional file 1: Figure S1, Table S1) and amorphous or in complex oxides such as clays and zeolites, is widely used in industry, scientific equipment, medicine, etc. [1–6]. Among different phases of alumina, corundum ($\alpha\text{-Al}_2\text{O}_3$) is characterized by very high hardness (equal to 9 according to Mohs scale), high melting point (2044 °C), and different colors when impurities are present (sapphires, etc.), i.e., corundum is of interest for various applications. In industrial production of $\alpha\text{-Al}_2\text{O}_3$, natural minerals such as bauxite, nepheline, and alunite are used in various processes [1–6]. Natural precursors are characterized by the presence of a variety of admixtures that make difficult production of pure aluminas. The use of pure precursors such as AlCl_3 in flame synthesis of alumina results in the formation of nanoparticles with a blend of different crystalline and amorphous phases

depending on the flame temperature and temperature gradient. If the flame temperature is higher than 1100 °C, then the content of $\alpha\text{-Al}_2\text{O}_3$ strongly increases; however, some other phases can be also present [7–9].

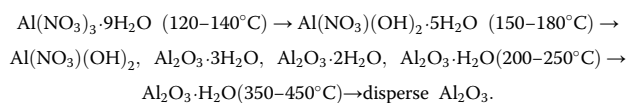
To prepare pure alumogel, liquid phase reactions are used with salt precursors such as $\text{Al}(\text{NO}_3)_3$, $\text{Al}_2(\text{SO}_4)_3$, and $\text{Al}(\text{OH})_2\text{Cl}$ [10–13]. Fast precipitation of the products of hydrolyzed salts of aluminum leads to formation of amorphous particles of alumogel [14]. Crystallization of alumogel in the aqueous media at room temperature occurs very slowly. In several months, crystallites of gibbsite ($\text{Al}(\text{OH})_3$) can form. Heating of alumogel at 98–100 °C gives boehmite ($\gamma\text{-AlO}(\text{OH})$) in 1 h. Precipitated alumogel is composed of small globules (5–10 nm in diameter) and fiber-like particles. Needle-like particles (whiskers) formed during 1 h are of 10–20 nm in thickness.

Stable sol of boehmite can be prepared by peptization of precipitant formed upon mixing the solutions of $\text{Al}(\text{NO}_3)_3$ and NH_4OH , and dried xerogel is macroporous [15, 16]. Another pathway of preparation of porous alumina using aluminum nitrate nonahydrate as a precursor is based on thermodestruction [17, 18]:

* Correspondence: mandzyuk_vova@ukr.net

¹Vasyl Stefanyk Precarpathian National University, 57 Shevchenko Street, 76018 Ivano-Frankivsk, Ukraine

Full list of author information is available at the end of the article



$\text{Al}(\text{OH})_2\text{NO}_3 \cdot \text{H}_2\text{O}$ formed at 150–155 °C and partial pressure of water vapor of 120–130 kPa can form stable colloidal solution in aqueous medium. Impregnation of ceramics by this solution and then calcination at 550 °C results in the formation of coating with $\gamma\text{-Al}_2\text{O}_3$. Water content (water vapor) can influence the processes of thermodestruction of crystalline aluminum hydrates. Therefore, it is of interest to study thermal transformations of aluminum nitrate nonahydrate in an atmosphere free of water vapor. The aim of this work was to study these processes in a flow-type reactor with Ar atmosphere, as well as the structure, morphology, and texture of aluminas prepared at different temperatures of calcination of the precursor with $\alpha\text{-Al}_2\text{O}_3$ as a final product.

Methods

The characteristics of the products of thermodestruction of aluminum nitrate nonahydrate (ANN) were studied for samples treated at 350, 480, 850, and 1100 °C in the Ar atmosphere (Table 1, samples 1, 2, 3, and 4, respectively). Thermodecomposition of ANN was studied using a STA 449F3 Jupiter (Netzsch) thermoanalyzer. Thermogravimetry (TG) gives changes in the sample mass (errors ± 1 mg), rate of changes in the mass (differential TG (DTG)), and enthalpy of the processes (differential thermal analysis (DTA), signal errors ± 0.05 μW). ANN was heated from 20 to 300 °C at a heating rate $\beta = 5$ °C/min, and partially dehydrated ANN ($\text{Al}(\text{NO}_3)_3 \cdot 7.5\text{H}_2\text{O}$) was heated from 20 to 1200 °C at $\beta = 10$ °C/min in the Ar flow at 30 ml/min.

The textural characteristics of samples were analyzed on the basis of low-temperature (77.4 K) nitrogen adsorption-desorption isotherms recorded using a Quantachrome Autosorb Nova 2200c adsorption analyzer. Before measurements, the samples were heated at 180 °C for

24 h. The specific surface area (S_{BET}) was calculated according to the standard Brunauer-Emmett-Teller (BET) method [19]. The total pore volume V_p was evaluated from the nitrogen adsorption at $p/p_0 \approx 0.99$, where p and p_0 denote the equilibrium and saturation pressure of nitrogen at 77.4 K, respectively [20]. The nitrogen desorption data were used to compute the pore size distributions (PSDs, differential $f_V(R) \sim dV_p/dR$ and $f_S(R) \sim dS/dR$) using a self-consistent regularization (SCR) procedure under non-negativity condition ($f_V(R) \geq 0$ at any pore radius R) at a fixed regularization parameter $\alpha = 0.01$ with a complex pore model with cylindrical (C) pores in alumina and voids (V) between spherical nonporous alumina nanoparticles packed in random aggregates (CV/SCR model) [21, 22]. The differential PSDs in respect to pore volume $f_V(R) \sim dV/dR$, $\int f_V(R)dR \sim V_p$ were re-calculated to incremental PSD (IPSD) at $\Phi_V(R_i) = (f_V(R_{i+1}) + f_V(R_i))(R_{i+1} - R_i)/2$ at $\sum \Phi_V(R_i) = V_p$. The differential $f_S(R)$ functions were used to estimate the deviation of the pore shape

from the model $\Delta w = \left(S_{\text{BET}} / \int_{R_{\text{min}}}^{R_{\text{max}}} f_S(R)dR \right) - 1$, where

R_{max} and R_{min} are the maximal and minimal pore radii, respectively [23]. The $f_V(R)$ and $f_S(R)$ functions were also used to calculate contributions of nanopores (V_{nano} and S_{nano} at $0.35 \text{ nm} < R < 1 \text{ nm}$), mesopores (V_{meso} and S_{meso} at $1 \text{ nm} < R < 25 \text{ nm}$), and macropores (V_{macro} and S_{macro} at $25 \text{ nm} < R < 100 \text{ nm}$). Additionally, the PSD were calculated using nonlocal density functional theory (NLDFT) method [24] using equilibrium model with cylindrical pores.

X-ray diffraction (XRD) patterns of samples 1–4 were recorded over $2\theta = 10^\circ\text{--}65^\circ$ range using a DRON-4-07 (Burevestnik, St. Petersburg) diffractometer with $\text{Cu K}\alpha$ ($\lambda = 0.15418 \text{ nm}$) radiation and a Ni filter. A copper X-ray source may preferentially produce a beam of X-rays with wavelengths 0.154 and 0.139 nm. Nickel has an absorption edge at 0.149 nm, between the two copper lines. Thus, using nickel as a filter for copper would result in the absorption of the slightly higher energy 0.139 nm X-rays, while letting the 0.154 nm rays through without a significant decrease in intensity. Thus, a copper X-ray source with a Ni filter can produce a nearly monochromatic X-ray beam with photons of mostly 0.154 nm. Analysis of the crystalline structure of aluminas was carried out using the JCPDS Database (International Center for Diffraction Data, PA, 2001) [25].

The infrared (IR) spectra of powdered samples over the $4000\text{--}300 \text{ cm}^{-1}$ range (at 4 cm^{-1} resolution) were recorded in transmittance mode using a Specord M80 (Carl Zeiss, Jena) spectrometer. Sample powders were stirred and pressed in a mixture with KBr (1:100, tables

Table 1 Conditions of preparation samples and their composition

Sample	Calcination temperature (°C)	Time of calcination (min)	Structural state	Phase composition
1	350	40	Amorphous	$\text{AlONO}_3 \cdot \text{H}_2\text{O}$ (90 %) AlOOH (10 %)
2	480	40	Amorphous/ crystalline	$\text{AlONO}_3 \cdot \text{H}_2\text{O}$ (30 %) AlOOH (70 %)
3	850	40	Amorphous/ crystalline	$\gamma\text{-Al}_2\text{O}_3$
4	1100	40	Crystalline	$\alpha\text{-Al}_2\text{O}_3$

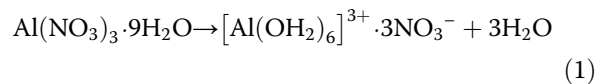
of ~20 mg). The spectra were re-calculated into the absorbance spectra.

A field emission-transmission electron microscope FE-TEM (JSM-2100F, Japan, voltage 200 kV) was used to record high-resolution TEM images of selected samples. A powder sample was added to acetone (for chromatography) and sonicated. Then, a drop of the suspension was deposited onto a copper grid with a thin carbon film. After acetone evaporation, sample particles remained on the film were studied with high-resolution transmission electron microscope (HRTEM).

Results and Discussion

Endo-effect (Fig. 1a, curve 3) in the range of 70–108 °C (maximum at 85 °C) shows melting of the

aluminum nitrate nonahydrate with parallel diminution of the sample weight (by 14 wt.% at 140 °C) due to water desorption. This process can be described by reaction



with removal of 3H₂O from ANN and formation of [Al(OH₂)₆]³⁺ bonding anions 3NO₃⁻. In the range of 140–210 °C, the weight diminution is 38 wt.% (16.8 wt.% in the range of 140–152 °C) due to process with endo-maximum at 158 °C due to removal of water and acid and formation of oligomer structures

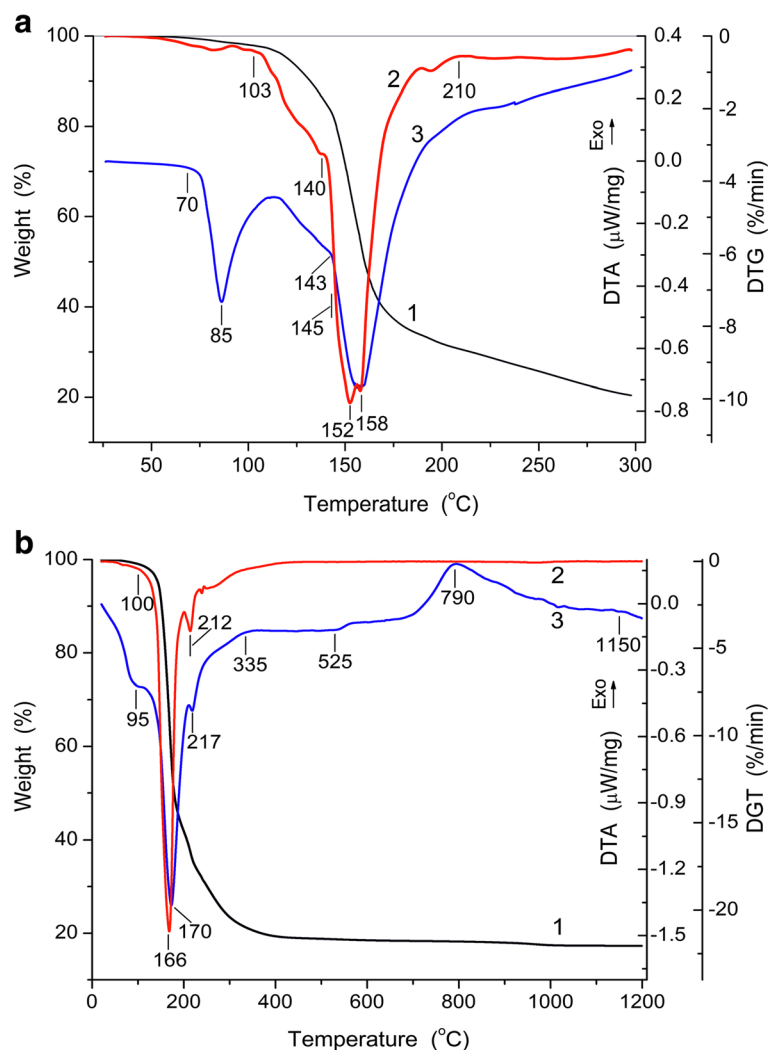
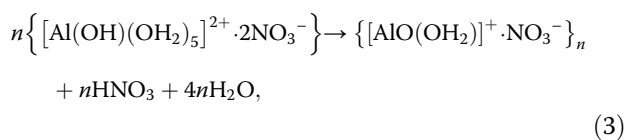
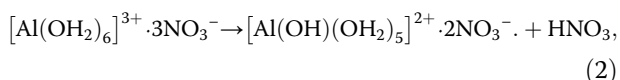
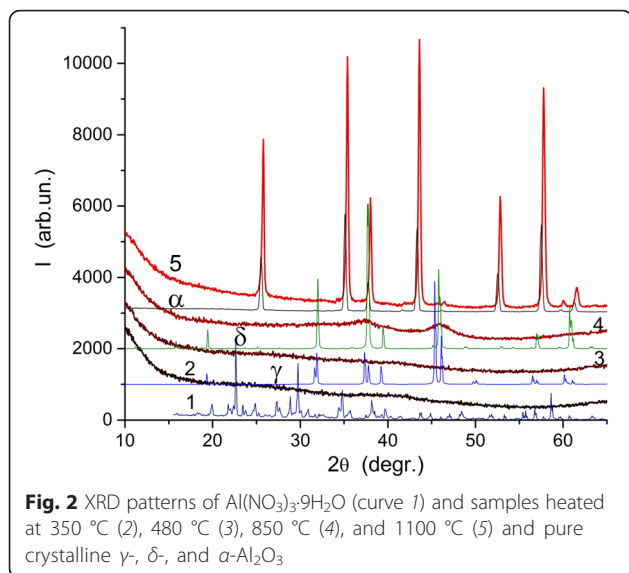


Fig. 1 TG (curves 1), DTG (2), and DTA (3) curves upon heating of Al(NO₃)₃·9H₂O to 300 °C at heating rate $\beta = 5$ °C/min (a) and Al(NO₃)₃·7.5H₂O to 1200 °C at $\beta = 10$ °C/min (b)



where $n = 3 \div 30$. In the oligomers, AlO₄ structures can be formed.

To enhance the DTA sensitivity at high temperatures in the mentioned processes, the amounts of water in the initial sample can be reduced from Al(NO₃)₃·9H₂O to Al(NO₃)₃·7.5H₂O due to preheating at 120 °C for 1 h. The TG/DTG/DTA study of the preheated sample upon heating to 1200 °C at $\beta = 10$ °C/min (Fig. 1b) shows that the increase in the value of β leads to a typical shift of the extreme toward higher temperature.

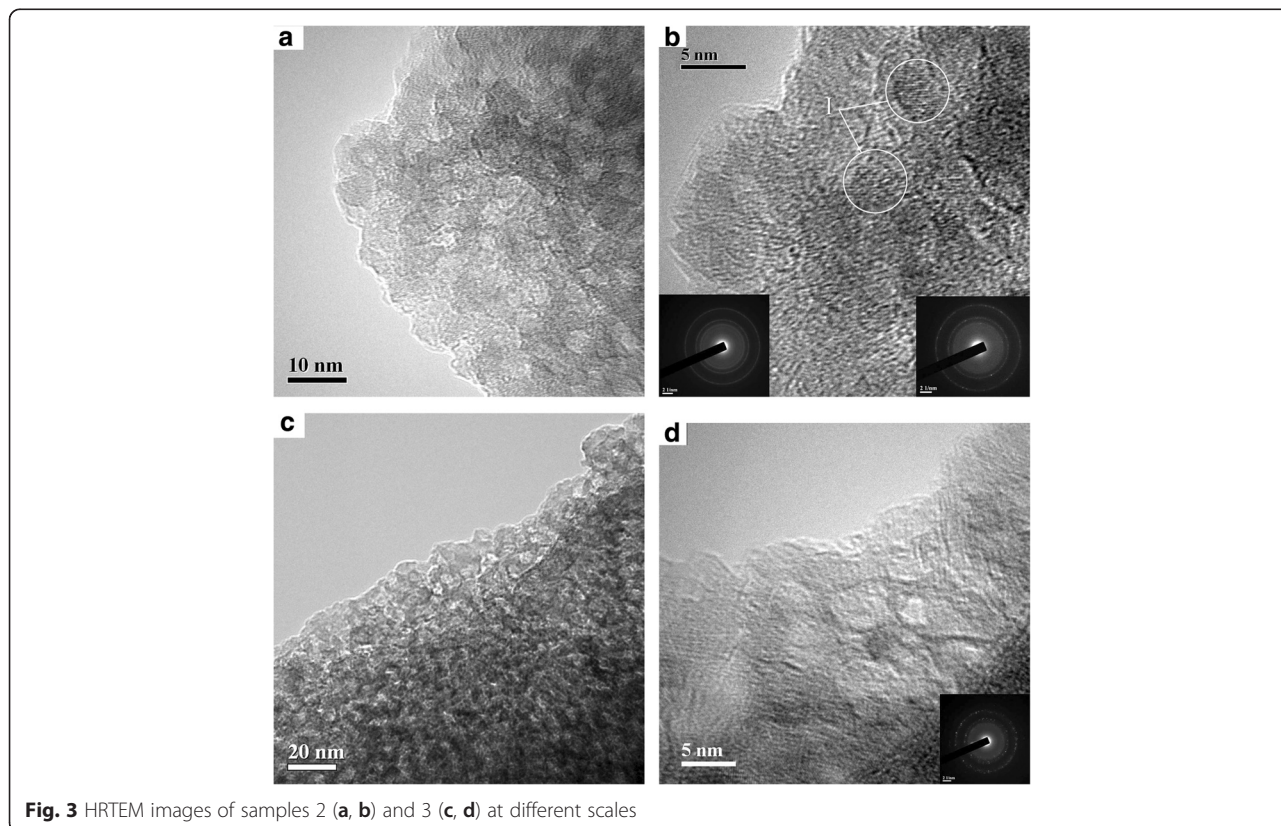
A small extremum of DTG at 212 °C (Fig. 1b, curve 2) and DTA at 217 °C is due to the removal of the HNO₃ molecules. In the 217–525 °C range, oligomers with [AlO(OH₂)]⁺·NO₃⁻ transform into aluminum hydroxide



The weight loss in this range is equal to 18 wt.%. The exo-effect (maximum at 790 °C) is due to transformation of aluminum hydroxide into oxide γ-Al₂O₃ at 525–1000 °C (see Additional file 1: Figure S1)



The endo-effect at $T > 1100$ °C is due to transformation of γ-Al₂O₃ into α-Al₂O₃ (Fig. 1b and in the Additional file 1: Figure S1).



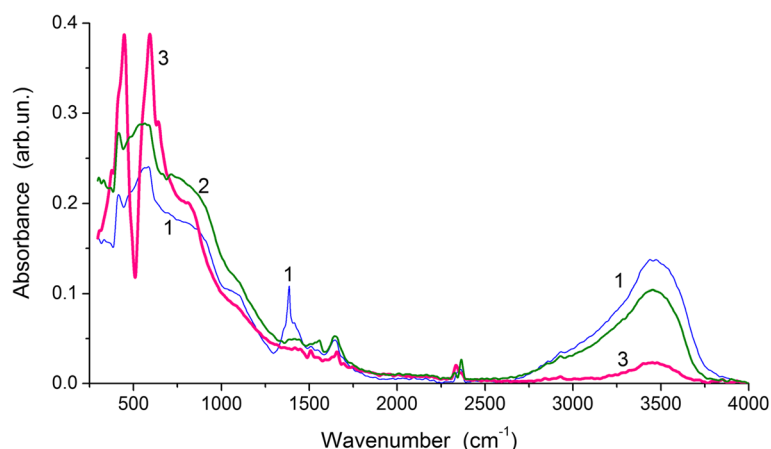


Fig. 4 IR spectra of samples 2 (curve 1), 3 (2), and 4 (3)

Changes in the phase composition of samples heated at different temperatures were studied using the XRD method (Fig. 2). The XRD pattern of sample 3 (Fig. 2, curve 4) shows appearance of crystalline nanoparticles and certain contribution of XRD amorphous alumina. According to the XRD patterns of pure crystalline aluminas (Fig. 2) and temperature ranges of stabilization of various aluminas (see Additional file 1: Figure S1), one can assume that the crystalline structures (formed upon heating at 850 °C) correspond mainly to γ - Al_2O_3 nanoparticles of 5–8 nm in size (Fig. 3c, d). A small size of them causes broadening of the XRD lines (Fig. 2). The lattice constant $a = 0.79431$ nm for sample 3 is larger than that for bulk γ - Al_2O_3 (see Additional file 1: Table S1). This effect is a consequence of nano-scaled size of crystallites with certain distortions in the surface layers of nanocrystallites (due to effects of the Laplace pressure and surface tension with decreasing particle size and increasing surface curvature) with great contribution of these layers into the volume of nanoparticles. Sample 4 prepared by calcination of ANN at 1100 °C is composed of α - Al_2O_3 crystallites (Fig. 2, curve 5) at lattice constants $a = b = 0.47579(5) \pm 0.00005(3)$ nm and $c = 1.29890(7) \pm 0.00012(7)$ nm.

Samples with ANN heated at 350 °C (Fig. 2, curve 2, $\text{AlONO}_3 \cdot \text{H}_2\text{O}$) and 480 °C (curve 3, AlOOH) are XRD amorphous. HRTEM images of sample 2 preheated at 480 °C (Fig. 3a, b) show nanoglobules of 6–10 nm in size, which are mainly amorphous and composed of the Al–O chains of 1–5 nm in length. However, some nanoparticles demonstrate crystalline structure (see Fig. 3b, marked structures).

The presence of oligomer (with unit $\text{AlONO}_3 \cdot \text{H}_2\text{O}$) chains with the Al–O bonds is confirmed by the IR spectra (Fig. 4). A band at 1385 cm^{-1} in the IR spectrum of sample 2 (Fig. 4, curve 1) is due to stretching vibrations of NO_3^- [26–28], and this band is absent in samples 3 and 4 undergoing heating at higher temperatures with removal nitro groups, i.e., pure alumina is formed.

The presence of both tetrahedral AlO_4 and octahedral AlO_6 structures in aluminas results in broadening of the Al–O stretching and deformation vibration bands including transverse (TO) and longitudinal (LO) optical components. The broad bands at $1100\text{--}650 \text{ cm}^{-1}$ and $650\text{--}300 \text{ cm}^{-1}$ can be roughly assigned to tetrahedral and octahedral structures in aluminas, respectively, with contributions of asymmetric (larger wavenumbers ν) and symmetric (smaller ν) vibrations. Corundum is mainly

Table 2 Textural characteristics of samples heated at 350 °C (1), 480 °C (2), 850 °C (3), and 1100 °C (4)

Sample	S_{BET} (m^2/g)	S_{nano} (m^2/g)	S_{meso} (m^2/g)	S_{macro} (m^2/g)	V_p (cm^3/g)	V_{nano} (cm^3/g)	V_{meso} (cm^3/g)	V_{macro} (cm^3/g)	Δw	$\langle R_V \rangle$ (nm)	$\langle R_S \rangle$ (nm)	c_{void}	c_{cyl}
1	66	29	37	0	0.044	0.009	0.035	0	0.153	1.94	1.28	0.392	0.608
2	180	34	146	0	0.138	0.007	0.131	0	0.470	1.97	1.65	0.697	0.303
3	77	6	71	0	0.086	0.001	0.080	0.005	0.397	8.14	2.44	0.536	0.464
4	14	3	9	2	0.070	0.001	0.032	0.037	0.292	33.55	10.39	0.538	0.462

Note. $\langle R_V \rangle = \frac{\int_{R_{\text{min}}}^{R_{\text{max}}} R f_V(R) dR}{\int_{R_{\text{min}}}^{R_{\text{max}}} f_V(R) dR}$; $\langle R_S \rangle = \frac{\int_{R_{\text{min}}}^{R_{\text{max}}} R f_S(R) dR}{\int_{R_{\text{min}}}^{R_{\text{max}}} f_S(R) dR}$; c_{void} and c_{cyl} are the weight coefficients corresponding to contributions of voids between spherical particles and cylindrical pores in CV/SCR

composed of octahedral AlO_6 structures with a small amount of AlO_4 in the surface layers and amorphous fragments. Sample 4 with corundum is the most ordered among all studied samples (Fig. 2). Therefore, the bands related to the Al–O stretching vibrations are narrower at $\nu < 700 \text{ cm}^{-1}$ linked to the AlO_6 structures (Fig. 4, curve 3) than those of samples 2 (curve 1) and 3 (curve 2). Additionally, relative contributions of bands at $\nu > 700 \text{ cm}^{-1}$ (linked to AlO_4 structures) decrease for sample 4.

Water is observed in all samples (a broad band of the O–H stretching vibrations at $3800\text{--}3000 \text{ cm}^{-1}$ and deformation vibrations at $1660\text{--}1650 \text{ cm}^{-1}$). However, its content decreases in a line of samples AlOOH (sample 2) $>$ $\gamma\text{-Al}_2\text{O}_3$ (3) $>$ $\alpha\text{-Al}_2\text{O}_3$ (4) because of a decrease in the specific surface area (Table 2, S_{BET}) and pore volume (V_p) resulting in diminution of water adsorption under the same conditions [9]. Weak bands at $1552\text{--}1514 \text{ cm}^{-1}$ can be attributed to HCO_3^- and CO_3^{2-} [29].

The textural characteristics of samples 1–4 (Table 2, Fig. 5) depend strongly on calcination temperature. Maximal porosity (Table 2, V_p) and specific surface area (S_{BET}) are characteristics for sample 2 calcined at $T_t = 480 \text{ }^\circ\text{C}$. Subsequent increase in the value of T_t results in a significant decrease in the porosity, especially for sample 4 treated at $T_t = 1100 \text{ }^\circ\text{C}$. Samples 1–3 have mainly narrow mesopores (Table 2, S_{meso} , V_{meso} , Fig. 5b, c) at small contribution of nanopores (S_{nano} , V_{nano}). Sample 4 possesses broad PSD (Fig. 5b, c) with increased contribution of macropores (S_{macro} , V_{macro}). Broadening of pores of samples with increasing calcination temperature is well observed in changes in the average pore radius in respect to pore volume (Table 2, $\langle R_V \rangle$) and specific surface area ($\langle R_S \rangle$). These changes can be explained by two effects. First, nanoglobules become smaller upon heating at higher temperatures due to removal of water, acid HNO_3 , or anions NO_3^- . Second, nanoparticles more strongly fuse with increasing temperature. The shape of pores is complex since the values of Δw (Table 2) characterizing the deviation of the pore model are large. Note that in the case of silica gels, the value of Δw can be much smaller up to $\Delta w \approx 0.01$ calculated using simple cylindrical pore model due to quite cylindrical shape of pores [9] in contrast to materials studied here (Fig. 2).

The investigation of phase-formation processes during thermolytic destruction of aluminum nitrate nonahydrate reveals new aspects of the synthesis of aluminum hydroxid-oxide and aluminum oxide compounds. Materials obtained in such way are nanostructured and chemically pure. They have specific physicochemical properties and may be used as adsorbents and catalyst carriers. It is possible to obtain single crystals of sapphire and ruby on its basis.

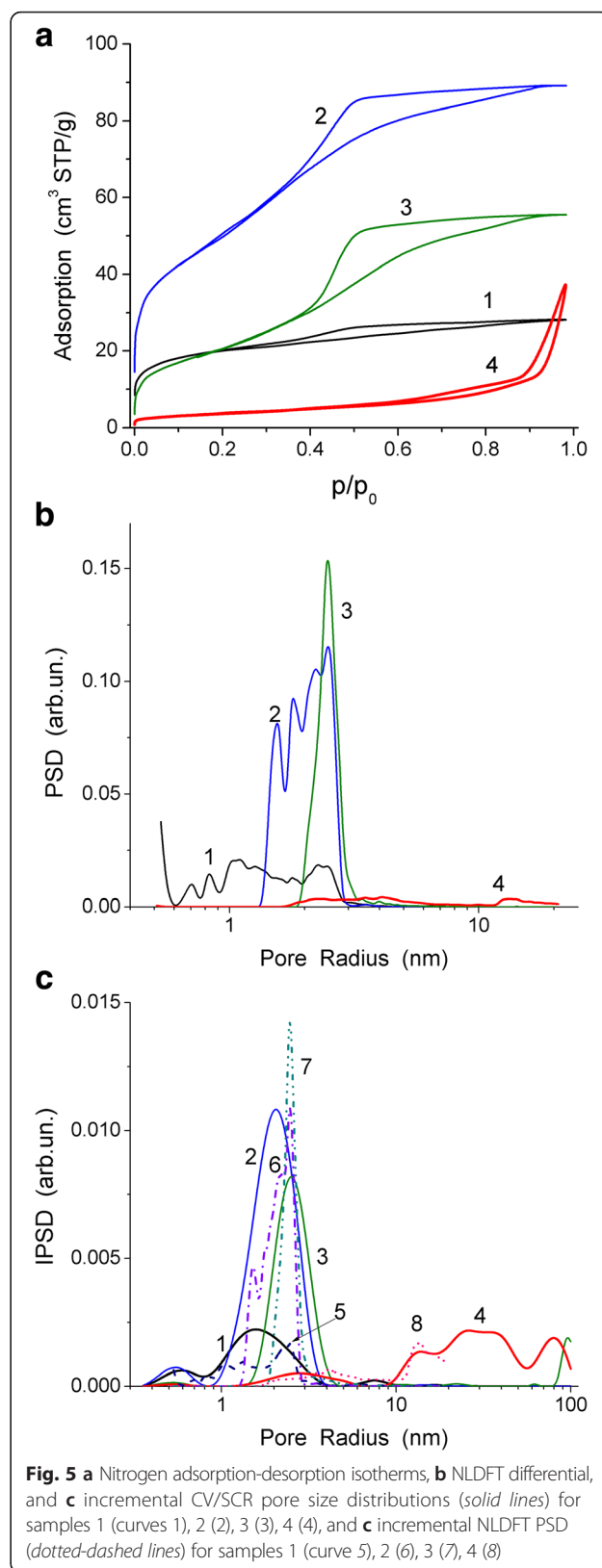


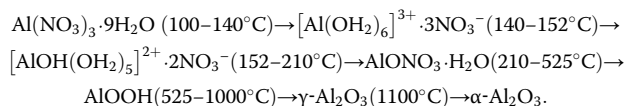
Fig. 5 a Nitrogen adsorption-desorption isotherms, b NLDFT differential, and c incremental CV/SCR pore size distributions (solid lines) for samples 1 (curve 1), 2 (2), 3 (3), 4 (4), and c incremental NLDFT PSD (dotted-dashed lines) for samples 1 (curve 5), 2 (6), 3 (7), 4 (8)

The complex water-soluble compound $[\text{AlOH}(\text{OH})_2]^{2+} \cdot 2\text{NO}_3^-$, formed in this process, was the convenient precursor to form secondary mesoporous Al_2O_3 -structure in silica-alumina ceramics by impregnation and calcination methods. Ceramics may be used as a membrane for ultrafiltration water purification after correction of the porous structure. This water-soluble compound is also used to form an active aluminum oxide layer on the surface of the cellular cordierite ceramic that is a carrier for the platinum-palladium catalyst.

In addition, nanostructured materials possess the properties strongly different from those of bulk materials, and this difference depends on the morphology of nanomaterials. Therefore, there is a fundamental problem to control the morphology of nanoparticulate materials, which tend to aggregate.

Conclusions

Investigations of calcination effects on the transformations of aluminum nitrate nonahydrate into boehmite, $\gamma\text{-Al}_2\text{O}_3$, and $\alpha\text{-Al}_2\text{O}_3$ show that it occurs according to scheme



Amorphous and crystalline phases of boehmite formed at $T > 210^\circ\text{C}$ represent nanoparticles of 6–10 nm in size strongly aggregated since $S_{\text{BET}} = 66 \text{ m}^2/\text{g}$ is smaller than it should be for unbound nanoparticles of the same sizes. In the amorphous phase, chains with $-\text{AlOH}-\text{O}-\text{AlOH}-$ have the length of 1–5 nm. Heating at 350–525 °C results in the formation of mesoporous aluminum hydroxide with decreasing size (2.5–5.0 nm) of nanoparticles. However, tight joining of these nanoglobules strongly reduces the specific surface area to 180 m^2/g instead of 350 m^2/g for individual spherical nanoparticles of similar sizes. Subsequent heating at 850 °C leads to enhanced binding of $\gamma\text{-Al}_2\text{O}_3$ nanoparticles in strongly aggregated structures, and S_{BET} drops down to 77 m^2/g . Corundum particles formed at 1100 °C are characterized by additionally increased joining in the aggregates because the value of S_{BET} is minimal (14 m^2/g).

Additional File

Additional file 1: Figure S1 and Table S1. Figure S1. Thermal transformation sequence of the aluminum hydroxides: gibbsite $\text{Al}(\text{OH})_3$, bayerite $\alpha\text{-Al}(\text{OH})_3$ and $\beta\text{-Al}(\text{OH})_3$, boehmite $\gamma\text{-AlO}(\text{OH})$, and diasporite $\alpha\text{-AlO}(\text{OH})$ into different phases χ , ρ , η , γ , δ , θ , and α -alumina characterized by different ranges of thermal stability. **Table S1.** Structural parameters of crystalline aluminas. (PDF 150 kb)

Abbreviations

ANN: aluminum nitrate nonahydrate; BET: Brunauer-Emmett-Teller; DTA: differential thermal analysis; DTG: differential thermogravimetry; HRTEM: high-resolution transmission electron microscope; IR: infrared; NLDFT: nonlocal density functional theory; PSD: pore size distribution; SCR: self-consistent regularization; TG: thermogravimetry; XRD: X-ray diffraction.

Competing Interests

The authors declare that they have no competing interests.

Authors' Contributions

IFM performed the problem definition, analyzed the IR spectra and HR TEM images, and participated in the discussion of experimental results. VIM stated the choice method and subjects of investigation, performed the XRD and low-temperature porometry experiments, and participated in the analysis and interpretation of data. VMS fabricated the initial standards and performed the TG/DTG/DTA experiment. VMG calculated the porous structure parameters of explored standards, participated in the analysis and interpretation of data, and wrote the paper. All authors read and approved the final version.

Authors' Information

IFM is the head of the Organic and Analytical Chemistry Department and a senior researcher at Vasyl Stefanyk Precarpathian National University, Ivano-Frankivsk, Ukraine. VIM is an associate professor at the Physics and Technology Department, Vasyl Stefanyk Precarpathian National University, Ivano-Frankivsk, Ukraine. VMS is a PhD student at the Organic and Analytical Chemistry Department, Vasyl Stefanyk Precarpathian National University, Ivano-Frankivsk, Ukraine. VMG is a professor, head of the Department of Amorphous and Structurally Ordered Oxides, Chuiko Institute of Surface Chemistry, Kyiv, Ukraine.

Acknowledgements

This work was supported by the Ministry of Education and Science of Ukraine (project no. 0113U001504c).

Author details

¹Vasyl Stefanyk Precarpathian National University, 57 Shevchenko Street, 76018 Ivano-Frankivsk, Ukraine. ²Chuiko Institute of Surface Chemistry, 17 General Naumov Street, 03164 Kyiv, Ukraine.

Received: 11 November 2015 Accepted: 10 March 2016

Published online: 22 March 2016

References

1. Patnaik P (2002) Handbook of inorganic chemicals. McGraw-Hill, New York
2. Levin I, Brandon D (1998) Metastable alumina polymorphs: crystal structures and transition sequences. *J Am Ceram Soc* 81:1995–2012
3. Wiberg E, Holleman AF (2001) Inorganic chemistry. Elsevier, Amsterdam
4. Hudson LK, Misra C, Perrotta AJ, Wefers K, Williams FS (2002) Aluminum oxide, in Ullmann's encyclopedia of industrial chemistry. Wiley-VCH, Weinheim
5. Gitzen WH (1970) Alumina as a ceramic material. The American Ceramic Society, Westerville
6. Ohring M (1992) The materials science of thin films. Academic, San Diego
7. Gun'ko VM, Zarko VI, Turov VV, Oranska OI, Goncharuk EV, Nychporuk YM, Pakhlov EM, Yurchenko GR, Lebeda R, Skubiszewska-Zięba J, Osovskii VD, Ptushinskii YG, Derzhypolskyi AG, Melenevsky DA, Blitz JP (2009) Morphological and structural features of individual and composite nanooxides with alumina, silica, and titania in powders and aqueous suspensions. *Powder Technol* 195:245–258
8. Gun'ko VM, Ilkiv VV, Zaulychnyy YV, Zarko VI, Pakhlov EM, Karpetz MV (2014) Structural features of fumed silica and alumina alone, blend powders and fumed binary systems. *J Non-Cryst Solids* 403:30–37
9. Gun'ko VM, Turov VV (2013) Nuclear magnetic resonance studies of interfacial phenomena. CRC Press, Boca Raton
10. Teagarden DL, Hem SL (1982) Conversion of aluminium chlorohydrate to aluminium hydroxide. *J Soc Cosmet Chem* 33:281–295
11. Park BK, Lee YS, Koo KK (2010) Preparation of highly porous aluminium hydroxide gels by hydrolysis of an aluminum sulfate and mineralizes. *J Ceram Proc Res* 11:64–68

12. McMillan PF, Diefenbacher JR, Petuskey WT, Goettler RW (2009) Water-soluble amorphous alumina-based ceramic precursors and alumosols: structural and chemical characterization. *J Non-Cryst Solids* 355:1539–1551
13. Zhu L, Pu S, Lu F, Liu K, Zhu T, Li J, Li J (2012) Preparation of dispersed aluminum hydroxide nanoparticles via non-aqueous route and surface modification. *Mater Chem Phys* 135:979–984
14. Okada K, Nogashima T, Kameshima Y, Yasumori A, Tsukada T (2002) Relationship between formation conditions, properties, and crystallite size of boehmite. *J Colloid Interface Sci* 253:308–314
15. Nazarov W, Pavlova-Verevkin OB (1998) Synthesis and colloid-chemical properties of hydrosols of boehmite. *Colloid J* 60:797–807
16. Pavlova-Verevkin OB, Rochinskaya YE (1993) Preparation and properties of stable sols of aluminum hydroxide. Study of peptization process of highly disperse aluminum hydroxide. *Colloid J* 55:133–137
17. Downs AJ (1993) Chemistry of aluminum, gallium, indium, and thallium, 1st edn. Chapman & Hall, London
18. Ismatov KP, Abdulaev AB (1970) On thermal decomposition of aluminum nitrate nonahydrate in the presence of water. *J Appl Chem* 43:668–670
19. Brunauer S, Emmett PH, Teller E (1938) Adsorption of gases in multimolecular layers. *J Am Chem Soc* 60:309–319
20. Gregg SJ, Sing KSW (1982) Adsorption, surface area and porosity. Academic, London
21. Gun'ko VM (2014) Composite materials: textural characteristics. *Appl Surf Sci* 307:444–454
22. Gun'ko VM, Lebeda R, Skubiszewska-Zięba J (2009) Heating effects on morphological and textural characteristics of individual and composite nanooxides. *Adsorption* 15:89–98
23. Gun'ko VM, Mikhailovsky SV (2004) Evaluation of slitlike porosity of carbon adsorbents. *Carbon* 42:843–849
24. Neimark AV, Ravikovitch PI (2001) Capillary condensation in MMS and pore structure characterization. *Micropor Mesopor Mater* 44/45:697–707
25. JCPDS Database. International center for diffraction data: PA; 2001
26. Farmer V (1974) The infrared spectra of minerals. Mineralogical Society, London
27. Klopogge JT, Wharton D, Hickey L, Frost RL (2002) Infrared and Raman study of interlayer anions CO_3^{2-} , NO_3^- , SO_4^{2-} and ClO_4^- in Mg/Al hydrotalcite. *Am Mineral* 87:623–629
28. Goebbert DJ, Garand E, Wende T, Bergmann R, Meijer G, Asmis KR, Neumark DM (2009) Infrared spectroscopy of the microhydrated nitrate ions $\text{NO}_3^-(\text{H}_2\text{O})_{1-6}$. *J Phys Chem A* 113:7584–7592
29. Su C, Suarez DL (1997) In situ infrared specification of adsorbed carbonate on aluminum and iron oxides. *Clay Clay Miner* 45:814–825

Submit your manuscript to a SpringerOpen[®] journal and benefit from:

- Convenient online submission
- Rigorous peer review
- Immediate publication on acceptance
- Open access: articles freely available online
- High visibility within the field
- Retaining the copyright to your article

Submit your next manuscript at ► springeropen.com
